

COMPARISON OF MHD MODELS FOR ALUMINIUM REDUCTION CELLS

V.Bojarevics and K.Pericleous
University of Greenwich, CMS, 30 Park Row, SE10 9LS, London, UK

Keywords: magnetohydrodynamics, waves, aluminium electrolysis, numerical modeling

Abstract

The self sustained waves at the aluminium-electrolyte interface, known as ‘MHD noise’, are observed in the most of commercial cells under certain conditions. The instructive analysis is presented how a step by step inclusion of different physical coupling factors is affecting the wave development in the electrolysis cells. The early theoretical models for wave development do not account for the current distribution at the cathode, instead assuming a uniform current density J_z at the bottom. When the electric current is computed according to the actual electrical circuit, the growth rate is significantly lower, and if a sufficient dissipation is included, does not lead to instability. The inclusion of the horizontal circulation-generated turbulence is essential in order to explain the small amplitude self-sustained oscillations. The horizontal circulation vortices create a pressure gradient contributing to the deformation of the interface. The full time dependent model couples the nonlinear fluid dynamics and the extended electromagnetic field that covers the whole bus bar circuit and the ferromagnetic effects.

Introduction

An electrolysis cell used to produce primary aluminium is sensitive to waves at the interface of liquid aluminium and electrolyte. It is recognised and exploited in mathematical modeling that the interface waves are similar to stratified sea layers dynamics [1]. However, for the case of electrolytic cells the penetrating electric current and the associated magnetic field are intricately involved in the oscillation process, which results in the observed wave frequencies being shifted from the purely hydrodynamic ones [2]. The interface stability problem is of great practical importance because the electrolytic aluminium production is a major electrical energy consumer, and it is related to environmental pollution rate. The first attempts of the stability analysis date back to [3,4] and a short summary of the main developments can be found in [2]. Important aspects of the multiple mode interaction have been introduced in [4]. Linear friction law for the wave motion and the horizontal circulation was first applied in [5] for the purpose of theoretical analysis, and it was widely used afterwards in theoretical studies. Actually, the linear friction is a simplification of the more general nonlinear bottom friction term appearing in the shallow water models, see for example [7]. The systematic perturbation expansion for the fluid dynamics and electric current problems, permitting reduction of the three-dimensional problem to the two-dimensional shallow layer problem was developed in [8], and the wave oscillation frequency shift with the magnetic interaction from the pure hydrodynamic state was mathematically proven. The procedure of the “shallow water approximation” can be extended for the case of weakly non-linear and dispersive waves using the Boussinesq formulation for non-unidirectionally

propagating waves at a two fluid layer interface in the presence of side walls [1]. Attempts to extend the electrolytic cell wave models to the weakly nonlinear case have started in [9] where the basic equations were derived, including the nonlinearity and linear dispersion terms. An alternative approach for the nonlinear numerical simulation for an electrolysis cell wave evolution is attempted in [10 and references there], by disregarding the dispersion terms and using the simple linear friction term.

The present paper contains a generalisation of the previous non-linear wave equations [9, 10] by accounting for the turbulent horizontal circulation flows in the two fluid layers and adding the nonlinear bottom friction law [7]. The inclusion of the turbulence model is essential in order to explain the small amplitude self-sustained, non-damped oscillations of the liquid metal surface observed in real cells, known as ‘MHD noise’. The fluid dynamic model needs to be fully coupled to the time dependent, extended electromagnetic simulation which includes not only the fluid layers, but the whole bus bar circuit and the ferromagnetic effects [11].

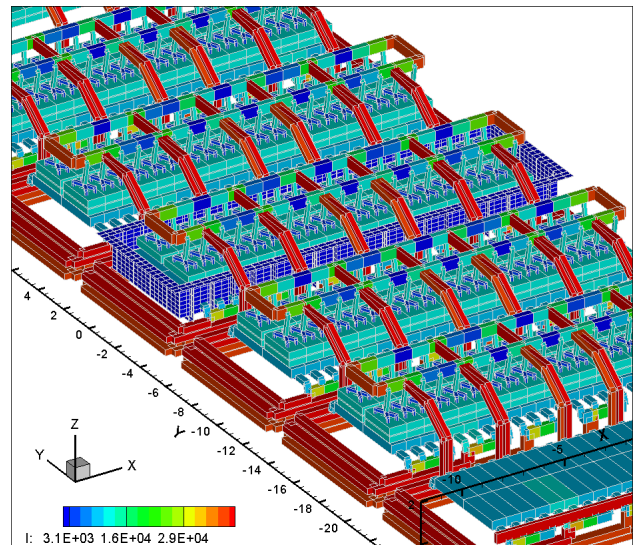


Figure 1. The electric current distribution in busbars for 500 kA cells in the potline. The test cell contains ferromagnetic shell.

Mathematical model reducing the 3d problem to shallow layer non-linear wave model

Aluminium reduction cells are arranged in a row of similar cells, where each cell is connected in series to the neighbours by a complex arrangement of current-carrying bus bars shown in

Figure 1 for a case of 500 kA side by side cells in line. The electric current to the individual cell is supplied from above via massive anode bus bars made of solid aluminium, from which anode rods connect to the carbon anodes. The liquid electrolyte layer beneath the anode blocks is relatively poor electrical conductor of a small depth (4-6 cm) if compared to its horizontal extension (3-4 m in width and 10-20 m in length). The electrolyte density ($\rho_2 = 2.1\text{e}3 \text{ kg/m}^3$) is of little difference to the liquid aluminium ($\rho_1 = 2.3\text{e}3 \text{ kg/m}^3$) pool bottom layer of typical depth 15–30 cm, created as the result of electrolytic reaction. The “shallow water” approximation assumes that the horizontal dimensions L_x and L_y are much larger than the typical depth H for each of the layers, and, in addition to this, the interface wave amplitude A is assumed to be small relative to the depth H . Thus the two small parameters of the problem are the nondimensional depth $\delta = H/L$ and the amplitude $\varepsilon = A/H$.

With the purpose to derive the Boussinesq equations for the wave motion we will need to estimate the terms in the full three-dimensional Navier-Stokes equations which are nondimensionalised with appropriate coordinate stretching to reveal explicitly the small parameters. The horizontal coordinates are made nondimensional by the horizontal length scale L and, according to the small depth assumption, a stretched vertical coordinate is

$$\bar{z} = z/(L\delta), \quad (1)$$

the nondimensional interface deformation of small amplitude are represented as

$$\bar{H}_0 = H_0/(L\delta) = \varepsilon \zeta(x, y, t). \quad (2)$$

The nondimensional variables are introduced using the following typical scales: the width of cell L for the horizontal coordinates x and y ; the typical gravitational wave velocity is scaled as $u_0 = \sqrt{gH}$, L/\sqrt{gH} for time t , $\rho_1 u_0^2$ for pressure p , IB_0/L^2 for the electromagnetic force \mathbf{f} (B_0 is typical magnetic field magnitude and I – the total electric current), the relative density $\rho = \rho_i/\rho_1$.

With these definitions the nondimensional fluid flow equations (continuity, horizontal momentum and vertical momentum) are represented respectively as:

$$\partial_k u_k + \delta^{-1} \partial_{\bar{z}} w = 0 \quad (3)$$

$$\rho(\partial_t u_j + u_k \partial_k u_j + \delta^{-1} w \partial_{\bar{z}} u_j) = -\partial_j p + \text{Re}^{-1}(\delta^{-2} \partial_{\bar{z}} v_e \partial_{\bar{z}} u_j + \partial_k v_e \partial_k u_j) + E f_j \quad (4)$$

$$\rho(\partial_t w + u_k \partial_k w + \delta^{-1} w \partial_{\bar{z}} w) = -\delta^{-1} \partial_{\bar{z}} p + \text{Re}^{-1}(\delta^{-2} \partial_{\bar{z}} v_e \partial_{\bar{z}} w + \partial_k v_e \partial_k w) + E f_z - \delta^{-1}, \quad (5)$$

where the summation convention is assumed over the repeating indexes k (equal to 1 or 2, respectively for x, y coordinates), v_e is the nondimensional effective turbulent viscosity, f_j are the components of electromagnetic force, and the last term in (5) represents the nondimensional gravity. The nondimensional governing parameters are the Reynolds number Re and the electromagnetic interaction parameter E :

$$\text{Re} = Lu_0/\nu, \\ E = (IB_0/L^2)/(\rho_1 u_0^2/L) = IB_0/(L^2 \rho_1 g \delta).$$

The Boussinesq equations can be derived formally if representing the velocity as an expansion in the small amplitude parameter:

$$\mathbf{u}(x, y, z, t) = \mathbf{u}_o(x, y, t) + \varepsilon \mathbf{u}_\varepsilon(x, y, z, t) + o(\varepsilon), \quad (6)$$

where \mathbf{u}_o is the horizontal circulation and \mathbf{u}_ε is the wave related velocity. An important feature of the shallow water approximation is the depth averaging procedure defined for the variables in each layer identified with number “ i ”. For example, the horizontal velocity component depth average is

$$\hat{u}_j(x, y, t) = (\bar{H}_i - \bar{H}_o)^{-1} \int u_j d\bar{z}, \quad (7)$$

and similar definitions are introduced for other depth dependent variables. The same depth averaging procedure formally can be applied to the fluid flow equations (3)-(5). The depth average of the continuity equation (3) for each of the two fluid layers ($i=1$ and 2) with the variable depths $\bar{H}_i(x, y, t)$ is

$$\varepsilon \partial_j \zeta = \partial_j [(\bar{H}_i - \varepsilon \zeta) \hat{u}_j], \quad (8)$$

which is accurate for all orders in ε , δ , and the kinematic boundary condition at the moving interface between the two liquids:

$$w(\bar{H}_o) = \varepsilon \delta \partial_j \zeta + \varepsilon \delta u_k(\bar{H}_o) \partial_k \zeta, \quad (9)$$

has been used to derive (8).

The continuity equation (3) and the condition (9) show that the vertical velocity expansion starts with the $\varepsilon \delta$ term:

$$w(x, y, z, t) = w(\bar{H}_o) - \delta [\partial_k \int_{\bar{H}_o}^{\bar{z}} u_k d\bar{z} + u_k(\bar{H}_o) \partial_k \bar{H}_o] \\ = \varepsilon \delta [\partial_j \zeta - \partial_k \int_{\bar{H}_o}^{\bar{z}} u_{ek} d\bar{z}].$$

Then the leading accuracy $O(1, \varepsilon, \delta)$ pressure expression can be derived from (5) as

$$p(x, y, \bar{z}, t) = p(x, y, \bar{H}_o, t) - \bar{z} + \varepsilon \zeta + \delta E \int_{\bar{H}_o}^{\bar{z}} f_z d\bar{z}.$$

When the depth averaging procedure (7) is applied to the horizontal momentum equations (4), the equations for the combined horizontal velocity (horizontal circulation \mathbf{u}_o , plus ε -order $\hat{\mathbf{u}}_\varepsilon$ wave motion) are

$$\hat{\mathbf{u}} = \mathbf{u}_o + \varepsilon \hat{\mathbf{u}}_\varepsilon \quad (10)$$

$$\rho(\partial_t \hat{u}_j + \hat{u}_k \partial_k \hat{u}_j) = -\partial_j p(\bar{H}_o) - \varepsilon \partial_j \zeta - \mu \hat{u}_j \\ + \text{Re}^{-1} \partial_k \bar{v}_e \partial_k \hat{u}_{0j} + E \hat{f}_j - \frac{1}{2} \delta E \bar{H}_i \partial_j f_{0z}, \quad (11)$$

where the continuity of the pressure at the interface is satisfied by introducing the pressure $p(\bar{H}_o)$ at the common interface. The effective turbulent viscosity $v_e(x, y, t)$ can be computed according to the depth averaged versions of empirical turbulence models. For our simulations we used a version of k - ω two equation model previously validated for other MHD flows [12]. The nonlinear

friction at the top and bottom of the fluid layers in (11) is defined similarly to general shallow water models [7]:

$$\mu \hat{u}_j = C_f |\hat{\mathbf{u}}| \hat{u}_j = \mathbf{Re}^{-1} \delta^{-2} (\bar{H}_i - \bar{H}_o)^{-1} \int \partial_z \bar{v}_e \partial_z u_j d\bar{z}. \quad (12)$$

The equations of momentum (11) and continuity (8) for the two fluid layers can be combined into a single nonlinear wave equation for the interface $\zeta(x,y,t)$ by taking the time derivative of (8), the horizontal divergence of (11). Then the difference between the resulting equations for the two layers permits to eliminate the common pressure at the interface $p(\bar{H}_0)$, yielding:

$$\begin{aligned} \varepsilon \langle \rho / \bar{H} \rangle \partial_t \zeta + \varepsilon \langle \mu \rho / \bar{H} \rangle \partial_z \zeta + \varepsilon \langle \rho \rangle \partial_{ij} \zeta = \\ E \langle \partial_j \hat{f}_j \rangle - \delta E \langle \frac{1}{2} \bar{H} \partial_{ij} \hat{f}_z \rangle \\ - \varepsilon \langle \rho / \bar{H} \partial_{ij} (\zeta u_{jo}) + \mu \rho / \bar{H} \partial_j (\zeta u_{jo}) \rangle - \langle \rho \partial_j (\hat{u}_k \partial_k \hat{u}_j) \rangle \end{aligned} \quad (13)$$

where $\langle F \rangle = F_1 - F_2$ denotes difference of the respective variable in the two layers and, for simplicity of presentation, μ is assumed as constant. The equation (13) formally is a generalization of the stability models used previously, from which the linear model [8] can be recovered by excluding the nonlinear and the dispersion terms [1]. The horizontal circulation velocities, driven by the rotational part of the electromagnetic force, can be calculated by solving the equation (11) in the two layers. The numerically efficient solution is to take the curl of the equation (11), then to rewrite it for the two dimensional horizontal flow stream function. The solution of the resulting 4th order equation for the stream function is sought in combination with the 2-equation turbulence model for the effective viscosity [12].

Results for different physical effects on the waves

In the following examples we will use the full electromagnetic model [11] suitable for realistic cell simulations. The proposed in [11] 500 kA cell configuration will be used in the course of this discussion. The magnetic field is computed from 6 cells in the potline (Fig. 1) and 4 cells in the return row (not shown). The magnetic field distribution is time dependent and recomputed at each time step of the flow and wave development. The typical distribution at the initial stage is shown in Figure 2 at the metal top level. The magnetic field variation is of an amplitude of about few Gauss and in this case is not affecting the cell stability (what is not always the case in general).

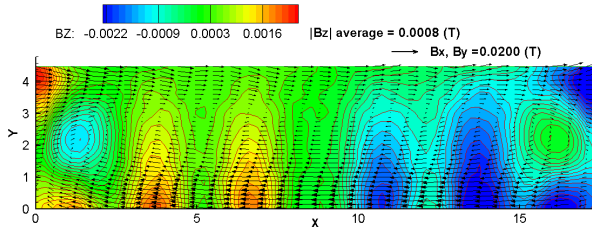


Figure 2. Magnetic field distribution in the 500 kA cell: contour lines for the vertical component Bz and vectors for the horizontal Bx and By field at the top of liquid metal.

The electric current distribution is computed in the fluid layers in conjunction with the external bus bar circuit [11], so that the waves affect the current redistribution in the anode bars, risers,

etc. The cathodic current distribution is mostly affected by the bus bar sizing design, the ledge position and remains practically time independent according to our observations from the model results. The electric current distribution in the liquid metal obtained from the present model is shown in Figure 3.

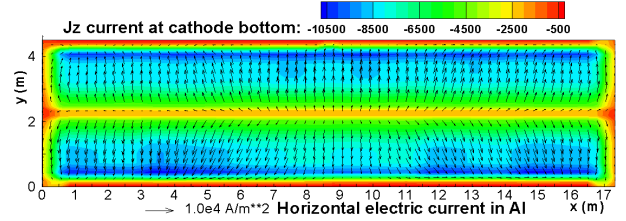


Figure 3. The electric current distribution in the liquid metal when the cathodic current is computed according to the busbar presence.

A typical simulation of the wave development starts with the flat aluminium-electrolyte interface. After the current distribution is obtained, the magnetic field is computed (with the steel parts included, requiring several iterations to converge for the nonlinear magnetic properties of the steel parts), and the resulting interface deformation is computed for the assumed 'stationary' state. This position of the interface is used as the initial condition to compute the current, magnetic field, turbulent horizontal velocities and the interface development for the full time dependent simulation. In addition, the anode bottom is gradually 'burnt out' in very small increments to accommodate to the time average interface position (replicating a real cell situation). This option can be disabled if required.

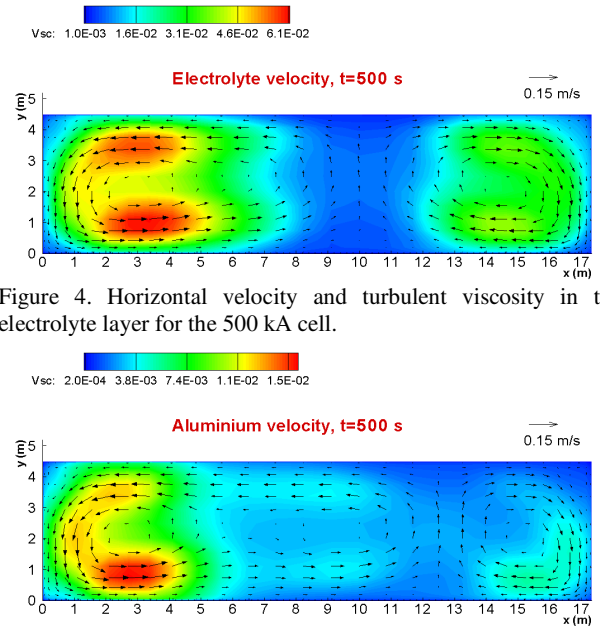


Figure 4. Horizontal velocity and turbulent viscosity in the electrolyte layer for the 500 kA cell.

Figure 5. Horizontal velocity and turbulent viscosity in the liquid aluminium layer for the 500 kA cell.

The velocity field is turbulent and time dependent. The horizontal, depth averaged circulation reaches almost stationary distribution, which is different in each of fluid layers mostly because of the electric current distribution variation. In the electrolyte layer the electric current from the individual anodes is passing predominantly vertically in this poorly conducting

material. The resulting flow is a rather symmetric vortex structure in the electrolyte layer (Fig. 4). The horizontal electric current in the aluminium, because of the cathodic bars, ledge and the wave perturbed interface, is responsible for the flow variation (Fig. 5), which is affected also by the magnetic field from the non-symmetric bus configuration compensating the return row. The horizontal circulation vortices create a pressure gradient contributing to the deformation of the free surface. Typically an intense vortex in a single fluid layer is associated with a surface dip in the vortex centre. For the two layers the effect on the common interface is in balance when two equal vortices are positioned one above the other because the last term in (13), responsible for the effect, is approaching zero as the densities of the two fluids are very close. Instructive comparisons can be made for the interface at the same time moments if accounting for the horizontal circulation and without the effect. Figure 6 clearly shows the dip at the centre where the vortex in aluminium is more intense. An elevation of the interface at the right side arises from the more intense electrolyte circulation in this region, as can be seen from comparing the Figures 4 and 5. The interface shape computed with the same parameters, except disabling the last term in equation (13), and keeping the same friction coefficient (12) with the turbulence effect on u_l , is shown in Figure 7. When the horizontal circulation effect in (13) is set to zero, the interface appears to be less deformed and the corresponding comparison of the self-sustained oscillation pattern is shown in Figure 8. Remarkably, the wave frequency, computed after the 1000 s simulation of the waves (Figure 9), is shifted from the pure gravitational waves as expected from the theory in [8] (see also [2] for comparison with real cell observation). The shift of frequencies is different in the two cases, with and without the horizontal circulation effect, suggesting the effect on the cell stability of the additional inclusion of the horizontal vortices in

the model. The effect of the vortices can be eliminated almost completely if making the vortices equal in both layers. A test run with the horizontal velocities made artificially equal in both layers confirms the interface shape similar to Figure 7. This observation can be an important tool for the more stable high amperage cell design where the horizontal magnetic field components, mostly responsible for the horizontal velocities, are usually not optimised.

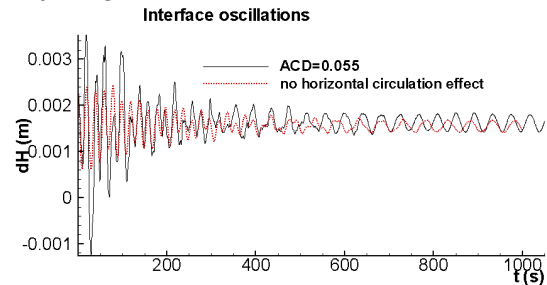


Figure 8. Comparison of the interface oscillations for the effect of the horizontal velocity circulation.

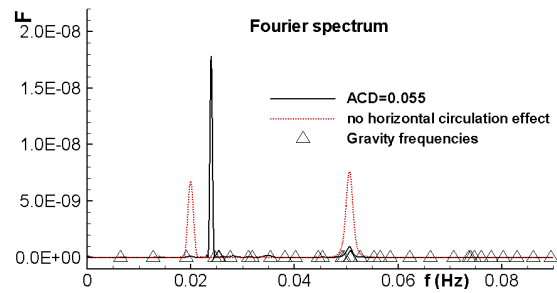


Figure 9. Fourier spectra for the interface oscillations with and without the horizontal circulation.

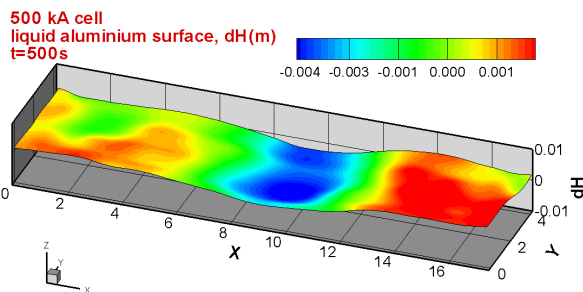


Figure 6. Interface at fixed time 500s when the cathode current is computed for the full busbar network, with the horizontal velocities effect.

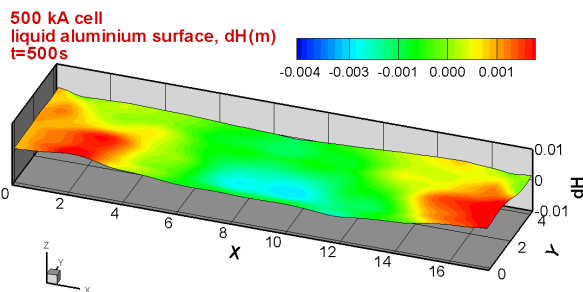


Figure 7. Interface at fixed time 500s when the cathode current is computed for the full busbar network, but the horizontal velocities effect on the interface is disabled.

With the present test bus bar configuration for the 500 kA cell and for the anode to cathode distance $ACD = 0.055$ m the level of the ‘MHD noise’ oscillations is very low (about 0.5 mm amplitude in a fixed position). The numerical model is very sensitive to the usual stability affecting parameters, like the depth of the liquid metal and the ACD. The cell becomes unstable if the metal depth is reduced from 0.30 m to 0.20 m, yet remains stable for 0.25 m even if the oscillation amplitude increases to 2 mm. Similarly, the decrease in ACD makes the cell unstable. The unstable interface computed for the $ACD = 0.035$ m is shown in Figure 10. The wave development pattern at a fixed interface location for different ACD is demonstrated in Figure 11. The unstable cell at $ACD = 0.045$ m demonstrates the frequency shift according to the mechanism described in reference [8].

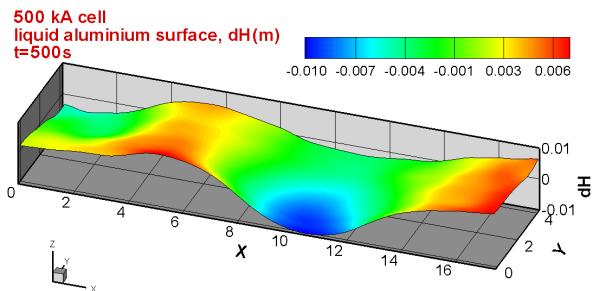


Figure 10. Initial development of instability in the unstable cell when the ACD is reduced to 0.035 m: interface at fixed time 500s.

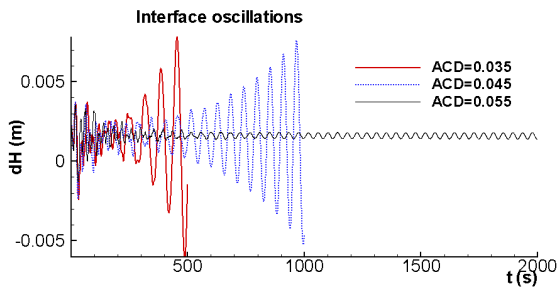


Figure 11. Comparison of the interface oscillations for different ACD: the cell becomes stable for ACD = 0.055 m.

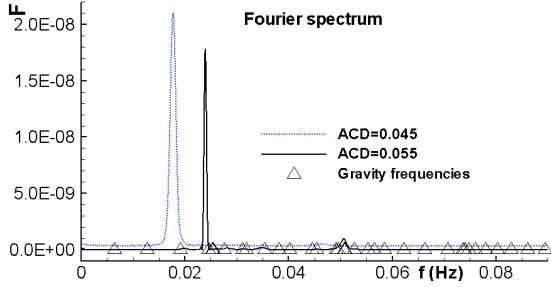


Figure 12. Fourier spectra for the interface oscillations with different ACD.

We mentioned previously the option in the full model of the gradual anode burnout at the bottom similar to the long term process in a real cell of the anode bottom accommodating to the more uniform average ACD. The previous results were obtained with this option enabled. What occurs if this option is disabled, as it is the case for simpler MHD models. The Figure 13 demonstrates a considerably different interface shape for the case without the anode burnout, and the Figure 14 - for the oscillation pattern. It is well known from the practical observations that the anode bottom burnout is nonuniform and this effect is important for the cell operation and the new anode setup procedure.

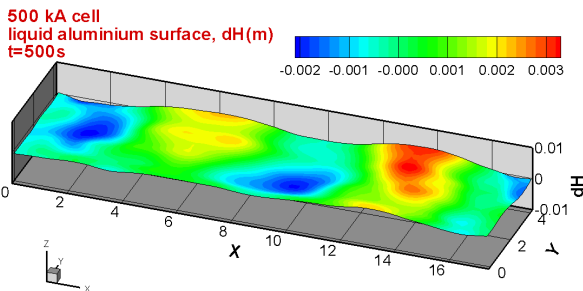


Figure 13. Interface at fixed time 500s when the anode burnout option is disabled (flat anode bottom).

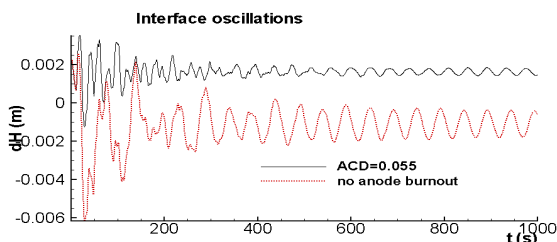


Figure 14. Comparison of the interface oscillations for the effect of the anode burnout.

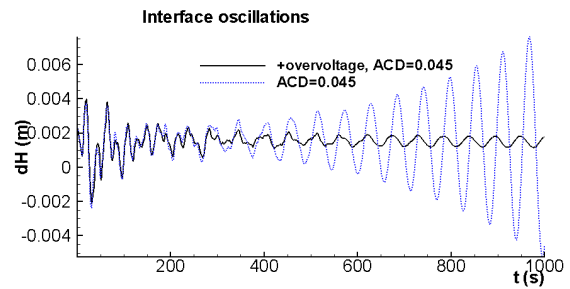


Figure 15. Comparison of the interface oscillations for the effect of the overvoltage variable part: the cell becomes stable for ACD = 0.045 m if part of the overvoltage is included.

The general model described in this paper permits a number of other important comparisons for the effect of different physical parameters. It includes also the user defined option for the parts of the polarization voltage which can be local current density dependent and can contribute to the irreversible voltage drop. Figure 15 demonstrates that if this part is included, the cell stability is improved, e.g., the 500 kA cell becomes stable at the ACD = 0.045 m. It is, of course, unstable for lower ACD values.

The next examples are illustrating what occurs if simpler models are used for the electric current calculation, as for instance in [3-6, 8-10], where typically the cathode current at the metal bottom is assumed to be $J_z = \text{const}$. Figure 16 shows the horizontal current distribution in this case, corresponding to the real anodes and the interface computed for this case (Figure 17). According to the simple models case we disabled anode burnout, the horizontal circulation and the additional overvoltage effects when computing these results. The corresponding computed interface oscillation is presented in the Figure 18 and the Fourier spectral analysis – in Figure 19. The oscillation spectra and pattern are quite different if the simpler models are used in comparison to the general model used in this paper and including various additional important physical factors.

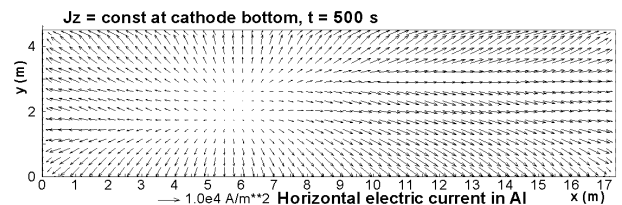


Figure 16. The electric current distribution in the liquid metal when the constant cathodic current condition is imposed.

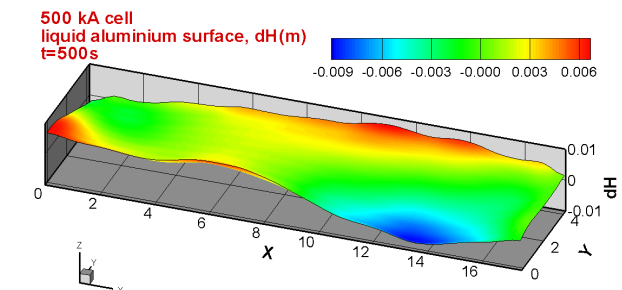


Figure 17. Interface at fixed time 500s when constant cathode current is given ($J_c = \text{const}$), and the horizontal velocities effect and the anode burnout are disabled.

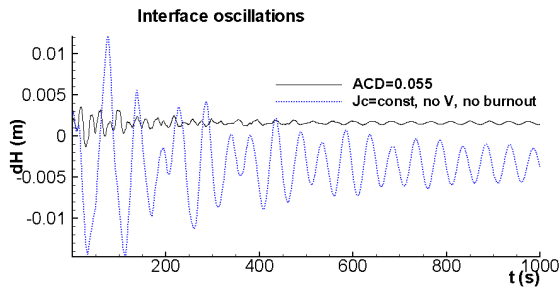


Figure 18. Comparison of the interface oscillations for the effect of the cathode current J_c distribution and the horizontal velocities effect and the anode burnout are disabled.

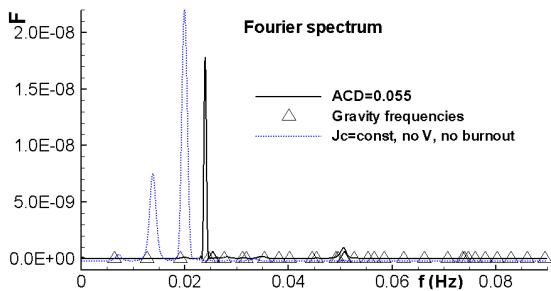


Figure 19. Fourier spectra for the interface oscillations with normally computed cathode current J_c distribution and the theoretical $J_c = \text{const}$ and the horizontal velocities effect and the anode burnout are disabled.

In the case if only the cathode current has been modified and other options kept the same as in the general model, the computed interface shape is still quite different from the previous (Figure 20) and the oscillation follows different pattern.

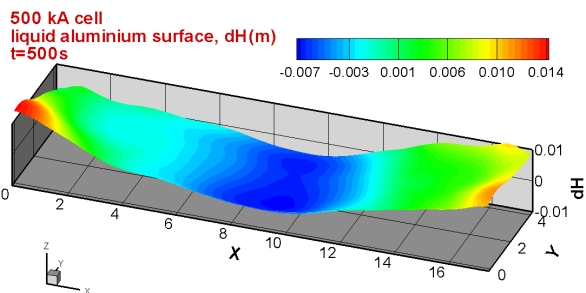


Figure 3. Interface at fixed time 500s when constant cathode current is given ($J_c = \text{const}$), with the horizontal velocities effect and the anode burnout.

Conclusions

The general MHD model including the nonlinear wave – horizontal circulation interaction gives results sensitively replicating the real cell behavior. The inclusion of various additional physical factors in the model are of importance for predicting the cell response to operation practice and the particular design elements. The model is user friendly and permits easily to simulate MHD response to various cell parameters.

References

1. C. C. Mei. *The Applied Dynamics of Ocean Surface Waves* (World Scientific, 1989).
2. R. Von Kaenel and J.P. Antille. Magnetohydrodynamic stability in alumina reduction cells. *Travaux*, 23 (1996), no. 27, 285-297.
3. Urata, N., Mori, K. and Ikeuchi, H. Behavior of bath and molten metal in aluminium electrolytic cell. *Keikinzo*, 26 (1976), no. 11, 573-600.
4. Th. Sele. Instabilities of the metal surface in electrolytic alumina reduction cells. *Metallurgical Transactions B*, 8B (1977), 613-618.
5. A. D. Sneyd and A. Wang. Interfacial instability due to MHD mode coupling in aluminium reduction cells. *J. Fluid Mech.*, 263 (1994), 343-359.
6. R. Moreau and J.W. Ewans. An analysis of the hydrodynamics of aluminium reduction cells. *Journal of Electrochemical Society*, 131 (1984), no. 10, 2251-2259.
7. A.K. Rastogi and W. Rodi. Prediction of heat and mass transfer in open channels. *J. Hydraulics Division ASCE*, HY3 (1978), 397-420.
8. V. Bojarevics and M. V. Romerio. Long waves instability of liquid metal-electrolyte interface in aluminium electrolysis cells: a generalization of Sele's criterion. *Eur. J. Mech., B/Fluids*, 13 (1994), no 1, 33-56.
9. V. Bojarevics. Nonlinear waves with electromagnetic interaction in aluminium electrolysis cells. *Progr. Fluid Flow Res.: Turbulence and Applied MHD. AIAA* (1998), Chapter 58, 833-848.
10. H. Sun, O. Zikanov, B. A. Finlayson and D. P. Ziegler. The influence of the basic flow and interface deformation on stability of Hall-Herault cells. *Light Metals 2005*, (TMS, 2005), 437-441.
11. M. Dupuis and V. Bojarevics. Weakly coupled thermo-electric and MHD mathematical models of an aluminium electrolysis cell. *Light Metals 2005*, (TMS, 2005), 449-454.
12. V. Bojarevics, K. Pericleous, R.A. Harding and M. Wickins. The Development and Validation of a Numerical Model of an Induction Skull Melting Furnace. *Metallurgical and Materials Transactions*, 35B (2004), 785-803.